Journal of Materials Chemistry A

ROYAL SOCIETY OF CHEMISTRY

PAPER

View Article Online
View Journal | View Issue

Check for updates

Cite this: J. Mater. Chem. A, 2022, 10, 13074

Improving the reducibility of CeO_2/TiO_2 by high-temperature redox treatment: the key role of atomically thin CeO_2 surface layers†

Ramón Manzorro, José M. Montes-Monroy, D. Goma-Jiménez, José J. Calvino, José A. Pérez-Omil * and S. Trasobares

CeO_2/TiO_2 catalysts treated in reaction environment at high temperatures evolve into complex and diverse systems, where several mixed oxides are formed. To analyze the redox behavior of this system, multiple oxidations and reducing thermal treatments have been applied. Results from the temperature-programmed reduction studies revealed a clear shift at lower temperatures on the reduction peak when the sample was previously reduced at high temperatures and oxidized under mild conditions. Meanwhile, the reduction peak was moved to high temperatures when the sample was previously reduced and oxidized at severe temperatures. The study, which was aimed at correlating this behavior with its chemical structure, was conducted using advanced electron microscopy, including high-resolution TEM and STEM imaging and spectroscopic techniques such as X-EDS and EELS. The data presented here comparing structures at the atomic level and chemical properties have uniquely unveiled that besides the cerium–titanium mixed oxides, a very thin layer up to a single monolayer was deposited along the TiO_2 surface, which indeed was responsible for the improvement of the reducing temperature.

Received 27th September 2021
Accepted 19th April 2022

DOI: 10.1039/d1ta08348a

rsc.li/materials-a

Open Access Article. Published on 09 June 2022. Downloaded on 12/9/2025 12:56:09 PM.
This article is licensed under a Creative Commons Attribution 3.0 Unported Licence.

Introduction

Among the catalyst supports, the CeO_2/ZrO_2 system has been extensively studied due to its relevance both as a catalyst and as a support of metal nanoparticles in a wide variety of processes related to environmental catalysis, particularly those linked to three-way catalysts and, more recently, the production of hydrogen for fuel cells (*e.g.* methane reforming,[1–3] water gas shift[4,5]) or CO_2 valorisation (*e.g.* dry reforming of methane). These mixed oxides depict outstanding redox and textural properties,[6,7] which are further enhanced/worsen after the application of thermal aging treatments under reducing and oxidizing atmospheres.[8,9] Such behaviour has been proved to be linked to the occurrence of order/disorder transitions at the cationic sublattice of the mixed oxide leading to the formation/destruction of a Ce/Zr oxidized pyrochlore phase, $Ce_2Zr_2O_8$, with higher oxygen release/exchange efficiency.[10,11]

Although being elements from the same group, there are structural and chemical differences between TiO_2 and ZrO_2, *e.g.* in terms of reducibility, it brings novelties to interactions with surface-type CeO_2 phases as well as new opportunities for the application of supported ceria systems. In fact, the higher availability, lower cost and chemical specificity of TiO_2, with respect to ZrO_2, have triggered several studies in the last few years on TiO_2-supported ceria, especially in the field of photocatalysis.[12–14]

A first differential aspect between these two related systems, of large interest in terms of material design, refers to the variety of mixed oxide phases in which the two elements (Ti, Ce) become mixed and ordered at the atomic level. In contrast with the CeO_2/ZrO_2 system, for which cationic ordering leads just to a pyrochlore type phase, the CeO_2/TiO_2 system displays a much more complex and flexible response to high-temperature thermal treatments.

In particular, a variety of compounds have been reported for the preparation of CeO_2/TiO_2 mixed oxides.[15–18] For example, Preuss *et al.*[19] reported the formation of three phases with different Ce/Ti stoichiometries, *i.e.*, Ce_2TiO_5 (orthorhombic), $Ce_2Ti_2O_7$ (monoclinic, with a layered perovskite structure) and $Ce_4Ti_9O_{24}$ (orthorhombic) after mixing the binary oxides (CeO_2 and TiO_2 or Ti_2O_3) under inert gas flow (argon) and at high temperatures (1200–1250 °C). Similarly, Gao *et al.*[20] reported the synthesis of monoclinic $Ce_2Ti_2O_7$ by submitting CeO_2 and TiO_2

Departamento de Ciencia de los Materiales e Ingeniería Metalúrgica y Química Inorgánica, Facultad de Ciencias, Universidad de Cádiz, Campus Río San Pedro, Puerto Real, 11510 Cádiz, Spain. E-mail: jose.perez-omil@uca.es

† Electronic supplementary information (ESI) available: Description of the thermal treatments applied to the samples, indicating the temperatures and gas flows. Structural information about the contact plane between CeO_2 and TiO_2. Characterization of the $Ce_2Ti_2O_7$ phase found after the SRMO treatments. ELNES spectra regarding the details of the Ti-$L_{2,3}$ fine structure. Atomic models depicting the arrangement of (111)-CeO_2 plane with A (1 layer) and ABC (3 layers) stacking. Ceria nanoparticle with fluorite structure on the CeO_2/TiO_2-SRSO-2C sample. SI performed on the CeO_2/TiO_2-SRSO-2C sample showing the ELNES structure for Ti-$L_{2,3}$ after harsh oxidation. See https://doi.org/10.1039/d1ta08348a

This journal is © The Royal Society of Chemistry 2022

Open Access Article. Published on 09 June 2022. Downloaded on 12/9/2025 12:56:09 PM.
This article is licensed under a Creative Commons Attribution 3.0 Unported Licence.

to a calcination treatment in argon at 1300 °C. As initially expected, when the reaction occurs under an oxidizing atmosphere, the resulting mixed oxide, $CeTi_2O_6$, assembles Ce^{4+} species. The calcination in the air has to be accomplished at mid-high temperatures, 700–1300 °C, if titanium and cerium nitrate are mixed,[21–23] or above 1300–1400 °C, when the binary oxides CeO_2 and TiO_2 are employed as precursors.[24]

Otsuka-Yao-Matsuo *et al.*[25] have also reported the synthesis of $CeTi_2O_6$ and $CeTiO_4$ through the oxidation of $Ce_4Ti_9O_{24}$ and $Ce_2Ti_2O_7$, respectively. The starting mixed oxides were obtained by direct calcination at 1200 and 1250 °C of a CeO_2–TiO_2 mixture under an Ar + 1% H_2 flow. The oxidation temperatures necessary to achieve $CeTi_2O_6$ and $CeTiO_4$ were 1000 °C and 400 °C, respectively. In the case of $CeTiO_4$, oxidation occurs *via* the accommodation of extra oxygen into the lattice, without modifying cerium and titanium cationic positions. In contrast, Gao *et al.*[20] reported segregation into CeO_2 and TiO_2 when $Ce_2Ti_2O_7$ was submitted to oxidation at 1100 °C. $CeTiO_4$ has also been prepared using molten salts, but cationic ordering was not confirmed.[26]

Importantly, as observed in the CeO_2/ZrO_2 system, Martos *et al.*[27] reported the synthesis of the pyrochlore type $Ce_2Ti_2O_7$ through the sol–gel method, starting from cerium nitrate and titanium isopropoxide as precursors and applying a reduction treatment at very high temperatures, 1200 °C.

The bulk-type Ce/Ti mixed oxide phases described above span the Ce : Ti molar ratio range from 2 : 1 to 0.5 : 1. This implies, in all cases, the use of large amounts of the lanthanide, which is currently classified as a critical element.[28] Indeed, from a catalytic point of view, targeting supported phases with low molar Ce contents has been demonstrated as a fruitful strategy to increase the efficiency in the usage of this lanthanide in heterogeneous catalysis. To accomplish the decrease of ceria loadings recommended as per the European Commission directive, it becomes interesting to deposit lanthanides on the TiO_2 surface[29–31] (where the catalytic reaction occurs), avoiding the presence of a bulk CeO_2 component.

In the particular case of materials supported on zirconia-based oxides, such as CeO_2/ZrO_2 or CeO_2/YSZ, the application of appropriate redox aging treatments, which include a high temperature reducing step, have been proven to transform the initial system of 3D CeO_2 nanoparticles dispersed on the support into extended ultrathin pyrochlore-type surface patches or layered nanostructures. In parallel, a significant improvement has been evidenced in the chemical behaviour. The supported systems have proved to present even a better redox behaviour, surpassing that of their respective bulk-mixed oxides of the same composition, as well as a better performance as catalyst supports.[32,33]

Herein, this approach is applied to a CeO_2/TiO_2 system in which ceria was incorporated in the molar loading amount required to prepare an ultrathin, just one monolayer thick, surface phase. We aimed not only to improve the redox behaviour of this poorly explored system but, importantly, to rationalize it in terms of the fine details of its structure.

In the case of the supported-CeO_2/TiO_2 system, the intrinsic complexity of the chemical system, where multiple mixed structures of varying cerium–titanium stoichiometries and different oxidation states may coexist, adds that related to the formation of surface nanostructures. Some of such phases could be present as atomically-thin layers, due to which, difficulties may be anticipated that may arise in the characterization of the actual structure of these nanomaterials, in which ceria is incorporated as a minority-supported phase.

As shown here, advanced structural and compositional characterization techniques, such as those available with the state-of-the-art aberration-corrected electron microscopes, which provide data with ultimate spatial and energy resolutions, are required to succeed in this quite challenging task.

Experimental section

To favour the distribution of CeO_2 on the surface of the TiO_2 crystallites, the starting TiO_2-supported CeO_2 material was prepared through microwave-assisted hydrothermal synthesis using 0.3 g of $Ce(NO_3)_3 \cdot 6H_2O$ (Alfa Aesar, 99.5% pure) and 1 g of TiO_2-P25 (Degussa, S_{BET} 60 $m^2\ g^{-1}$). The 0.3 g of cerium nitrate used for the deposition corresponds to the mass estimated as necessary to cover the TiO_2 surface with a CeO_2 monolayer. The cerium precursor and TiO_2 powder were added to 60 ml of water. The corresponding aqueous suspension was stirred for 30 minutes and then the pH was increased to 10 by the addition of ammonium hydroxide (Merck, 25%) to accomplish cerium precipitation. The mixture was then transferred to a Teflon reactor and deposited into a microwave oven (ETHOS One, Milestone), where it was heated up to 180 °C for 20 minutes (350 W). The resulting product was filtered, dried for 24 hours and calcined at 500 °C for 1 hour to eliminate potential nitrates. This sample was labelled as CeO_2/TiO_2-fresh. An actual cerium loading of 8 wt%, was determined using inductive coupled plasma-atomic emission spectroscopy (ICP-AES), which corresponded to that estimated for a CeO_2 monolayer coverage of the total surface available on the TiO_2 support used in the preparation.

A portion of the CeO_2/TiO_2-fresh sample was submitted to redox aging cycles aimed at promoting the formation of Ce/Ti mixed oxide phases and modifying their nanostructure. In particular, severe reduction mild oxidation (SRMO) and severe reduction severe oxidation (SRSO) treatments were applied. In both cases, the severe reduction (SR) step consisted of heating the sample up to 850 °C under an H_2 (5%)/Ar flow, keeping it at that temperature for 1 hour, cooling it down to 500 °C under the reducing atmosphere and, finally, switching the gas flow to pure He to allow the sample to cool to room temperature. Under severe and mild oxidation (SO and MO, respectively) treatments, the samples were heated under an O_2 (5%)/He flow, up to 850 °C in the first case and only up to 500 °C in the later case, for 1 hour. SRMO and SRSO treatments were applied consecutively. Thus, after the SRMO treatment, the sample was named CeO_2/TiO_2-SRMO-1C. The application of the SRSO treatment to this one leads to a sample named as CeO_2/TiO_2-SRSO-2C sample. Finally, the sample resulting from the application of additional SRMO treatment, after SRSO, results in the CeO_2/TiO_2-SRMO2-

Open Access Article. Published on 09 June 2022. Downloaded on 12/9/2025 12:56:09 PM.
This article is licensed under a Creative Commons Attribution 3.0 Unported Licence.

3C sample. Fig. S1† illustrates a scheme of the treatment protocol just described.

To evaluate the reducibility of CeO_2/TiO_2 catalysts, temperature-programmed reduction experiments were performed using a Pfeiffer quadrupole mass spectrometer, model Thermostar QME-200-D-35614. For these TPR-MS experiments, 200 mg of the sample was placed in a quartz tube U-shaped reactor. Prior to TPR-MS measurements, the samples were subjected to a surface cleaning step, which consisted of heating it to 500 °C under O_2 (5%)/He flow at 60 cm^3 min^{-1}, keeping the sample at that temperature for 1 hour, and further cooling to 150 °C under the same gas mixture. At this temperature, the flow was switched to He and the sample was finally cooled to room temperature. The TPR-MS analyses were performed under H_2 (5%)/Ar, using a flow rate similar to that used during the oxidizing cleaning step. For a consistent analysis of the TPR-MS experiment, both the evolution of water (mass/charge ratio = 18) and H_2 consumption (mass/charge ratio = 2) were followed. To provide quantitative results about the reduction degree of Ce in the CeO_2/TiO_2-fresh and CeO_2/TiO_2-SRMO-1C catalyst, additional experiments were performed, following the aforementioned protocol, using an Autochem II 2920 (Micromeritics), equipped with a thermal conductivity detector (TPR-TCD).

Carbon-coated copper grids were used to deposit the ground powder of CeO_2/TiO_2 catalysts and were characterized using a variety of complementary advanced electron microscopy techniques, using a double aberration-corrected monochromated FEI TITAN Cubed Themis 60–300 TEM/STEM microscope, operating at 200 and 80 kV (C_s = 0.001 mm and sub angstrom resolution). Structural analysis and the phase identification of the binary and ternary oxides present in the different samples were performed by acquiring high-resolution images both in TEM (HRTEM) and high angle annular dark field STEM imaging (HR-HAADF) modes. STEM-HAADF images, in which the brighter contrast corresponds to atomic columns containing Ce due to its higher Z number ($Z_{Ce} = 58$ *versus* $Z_{Ti} = 22$ or $Z_O = 8$), in combination with analytical techniques such as X-ray energy dispersive spectroscopy (X-EDS) or electron energy loss spectroscopy (EELS) has allowed us to determine the spatial distribution of the different elements with atomic resolution, identifying the phases present and, also, exploring the oxidation states of the cations from the analysis of the energy loss near edge structure (ELNES). STEM X-EDS experiments were also performed using the Super X-G2 capabilities of the microscope, using a beam current in the 120–140 pA range and a dwell time per pixel of roughly 100 μs. X-EDS elemental maps were obtained by monitoring the Ce-L (4.84 eV) and Ti-K (4.51 eV) lines. To further improve their visualization, a Gaussian blur of 0.8 post-filter was employed, accessible in the Velox software. On the other hand, the EELS data for the Ce-$M_{4,5}$ (883 eV) and Ti-$L_{4,5}$ (456 eV) edges were acquired working in the so-called spectrum-imaging (SI) mode,[34] which allows a direct correlation of the structural and analytical information on the analysed regions, collecting simultaneously at every pixel the HAADF and EELS signals. In these EELS experiments, the DUAL EELS mode was used, in which the zero-loss and the core-loss regions were simultaneously recorded, enabling a rigorous determination of the absolute value of the energies at which the core-loss signals appeared. Elemental identification and quantification tasks of EELS experiments were performed with 0.25 eV ch^{-1} energy dispersion (reaching an energy resolution of 0.9–1 eV), 50–70 mrad of collection semi-angle, 60 pA probe current and 50 ms acquisition time per EELS spectrum. More demanding conditions were used for the analysis of the ELNES structure. In this particular case, 0.1 eV energy resolution was accomplished through the use of a 1.0 excitation of the monochromator and much lower energy dispersion, 0.025 eV ch^{-1}. Moreover, 30–50 mrad of the collection angle, 50 ms acquisition time per EELS spectrum and currents below 30 pA were used to avoid any beam-induced modification of the oxidation state of cerium or titanium species. Prior to analysis of the elemental maps or the fine structure, the background was removed from raw data through a power-law model and an energy window width of 25 eV.

The analysis of the experimental high-resolution images was performed by comparing the simulated STEM-HAADF images, obtained using the TEM-SIM software[35] and the following experimental conditions were applied: accelerating voltage = 80 kV; C_s = 0.001 mm; C_5 = 5 mm; Δf = 2–4 nm and a HAADF detector geometry covering the dispersion angle range from 80 to 200 mrad. To further approach the contrasts observed in the experimental images, the simulated images were blurred using a Gaussian filter with a sigma value of 2. Similarly, the electronic noise with a standard deviation of 25% was also applied.

EELS elemental map simulations were performed using the μ-STEM software[36] and employing the following electron-optical parameters: 16 mrad convergence angle, 1 nm defocus, 0.001 mm C_s, 5 mm C_5, 36.7 mrad collection angle and 30 eV energy threshold.

For the interpretation of the experimental atomic resolution images, the Eje-Z software[37] present at TEM-UCA server[38] was also used. The structural models required to perform image simulations were built using the Rhodius software,[39] which allows precise control of morphological, structural and crystallographic orientation features.

To complement the nanoscopic view provided using the electron microscopy techniques, surface analysis at the macroscopic level was also performed by X-ray photoelectron spectroscopy (XPS). The spectra were recorded in a Physical Electronics PHI 5701 spectrometer, with a take-off angle of 45° and Al Kα monochromatic radiation (1486.6 eV). Given the low loading of the lanthanide, the exposure time was set to 105 minutes to achieve a SNR which allowed reliable and precise quantification of the Ce/Ti molar ratio, monitoring Ce 3d and Ti 2p signals. For the determination of the Ce^{3+}/Ce^{4+} oxidation state ratio, a much shorter acquisition time was used, 8 min, since the optimization of SNR and avoidance of X-ray damage effects is necessary, given the high susceptibility of Ce^{4+} to be reduced.[40,41] To quantify the contribution of each oxidation state, the spectra were deconvoluted following the procedure described elsewhere.[42] To further explore the nature of the ultrathin Ce layers, angle-resolved XPS experiments were employed, recording a series of spectra in the 15 to 75° angle range, using in this case Mg Kα radiation (1253.6 eV).

 This journal is © The Royal Society of Chemistry 2022

Open Access Article. Published on 09 June 2022. Downloaded on 12/9/2025 12:56:09 PM.
This article is licensed under a Creative Commons Attribution 3.0 Unported Licence.

Results and discussion

Redox performance

Before describing the redox behaviour of the CeO_2/TiO_2 samples, it should be stated that bare CeO_2 is a well-known reducible material, showing a typical temperature-programmed reduction (TPR-MS) profile with two major reduction peaks. A first one at ~500 °C and a second, broad one, above 800 °C. These have been ascribed to the surface and bulk-related reduction events.[43,44] In the case of TiO_2-P25, a less reducible oxide in our working conditions, the profile shows a very small reduction degree, which is almost negligible once ceria was added (Fig. S2†).

The TPR-MS profiles corresponding to the CeO_2/TiO_2-fresh, CeO_2/TiO_2-SRMO-1C, CeO_2/TiO_2-SRSO-2C and CeO_2/TiO_2-SRMO2-3C samples are shown in Fig. 1. Different features were clearly observed, indicating an influence of the thermal treatments on the redox response. Thus, in CeO_2/TiO_2-fresh catalysts, the reduction is initiated at 360 °C and it extends up to 800 °C, with two broad peaks at roughly 575 and 700 °C. A very significant change is observed after the first SRMO treatment. In CeO_2/TiO_2-SRMO-1C reduction starts at a similar temperature (350 °C), but is mostly completed in a single peak centered at 485 °C and ending at 570 °C. Therefore, the reduction shifts to lower temperatures with respect to the CeO_2/TiO_2-fresh sample. Only a minor reduction event is observed at the higher temperature, roughly at 620 °C. It is also evident that the SRSO aging cycle largely deteriorates the redox response at a low temperature of the catalyst with respect to both the as-prepared one and, more importantly, the CeO_2/TiO_2-SRMO-1C sample. The TPR-MS profile of the CeO_2/TiO_2-SRSO-2C catalyst shows a very broad and asymmetric reduction event, which spans the high-temperature range (600–900 °C) and peaks at 840 °C.

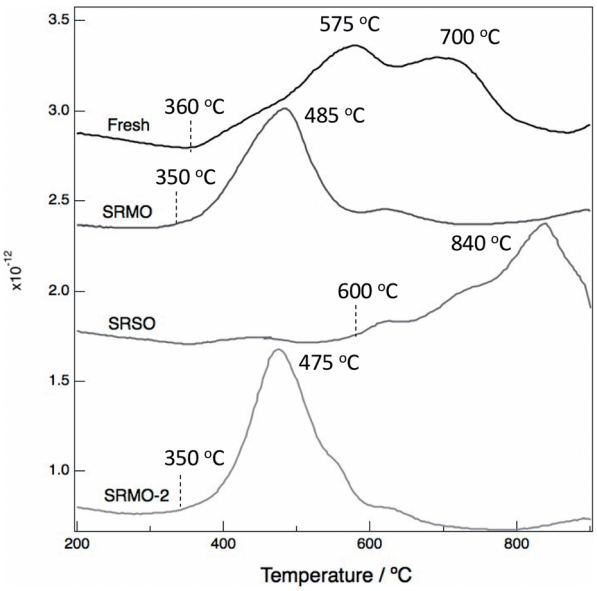

Fig. 1 From top to bottom, temperature programmed reduction (TPR-MS) corresponding to CeO_2/TiO_2-fresh, CeO_2/TiO_2-SRMO-1C, CeO_2/TiO_2-SRSO-2C and CeO_2/TiO_2-SRMO2-3C.

Interestingly, the application of a second SRMO treatment to the previous sample reverts the redox response of the catalyst and leads to a material that is reducible at low temperatures. In fact, CeO_2/TiO_2-SRMO2-3C exhibits a reduction profile quite comparable to that of CeO_2/TiO_2-SRMO-1C, with a single peak centered at 475 °C. A comparison with pure CeO_2 samples reported in the literature suggests that, after the SRMO treatments, CeO_2/TiO_2 experience reduction as a pure surface phase, since the high-temperature peak corresponding to the bulk reduction is not observed.

To evaluate from a quantitative point of view, the fraction of cerium being reduced after each redox cycle, the total areas under different plots in Fig. 1 were measured and compared to those of the CeO_2/TiO_2-fresh catalyst. If a full reduction of the Ce^{4+} content of this sample is assumed, the ratios of the obtained TPR-MS profile area indicate the degree of reduction for CeO_2/TiO_2-SRMO-1C and CeO_2/TiO_2-SRMO2-3C amounting to 71% and 86%, respectively. This result suggests that although the redox response improves after the SRMO treatments, by shifting the major reduction peak to lower temperatures, there is a certain fraction of cerium (29% for the first and 14% for the latter) that remains trapped in a reduced state, *i.e.*, as Ce^{3+}, after the mild oxidation.

To reach a more precise quantification of the fraction blocked in the reduced Ce^{3+} state, quantitative TPR experiments were performed on different samples, using an experimental system based on a TCD (TPR-TCD), Fig. S2 and S3.† Thus, H_2 consumption values of 0.06, 0.35 and 0.22 mmol were measured for bare TiO_2, CeO_2/TiO_2-fresh, and CeO_2/TiO_2-SRMO-1C samples, respectively. Taking into account the hydrogen consumption of bare TiO_2, these values indicate a full reduction of ceria in the case of the fresh sample (0.29 mmol g^{-1} ideally) and a lower reduction degree in the case of the SRMO sample, 0.16 mmol. Then, it becomes clear that in the fresh sample Ce is fully oxidized, whereas in the SRMO catalyst about 45% of the total cerium mass is present as Ce^{3+}, which can be considered a more accurate value of the actual redox state of the lanthanide than that estimated from the TPR-MS results.

In the case of the CeO_2/TiO_2-SRSO-2C sample, the area ratio in TPR-MS indicates a total Ce^{4+} content of 97%. According to this, oxidation at high temperature is necessary to transform the whole Ce^{3+} content of the catalyst back into Ce^{4+}, although in this transformation, the material experiences a significant deterioration of its redox performance.

The results commented up to this point clearly reveal that the redox behaviour of CeO_2/TiO_2 mimics that previously observed in CeO_2/ZrO_2,[33] in the sense that a fully reversible switch between states of improved and deteriorated reducibility can be triggered by applying redox aging treatments under high temperature reducing and oxidizing conditions, respectively. Moreover, previous results on CeO_2/ZrO_2 and CeO_2/YSZ suggest that reversibility would be extended to further SRMO–SRSO cycles. Nevertheless, as shown by the in-depth analysis presented in the following sections, the structural roots of this peculiar behaviour neatly differ from those of CeO_2/ZrO_2.

Open Access Article. Published on 09 June 2022. Downloaded on 12/9/2025 12:56:09 PM.
This article is licensed under a Creative Commons Attribution 3.0 Unported Licence.

Catalyst nanostructure

To clarify the structural modifications occurring after the redox aging treatments, detailed and thorough advanced electron microscopy characterization was carried out. In this context, imaging (HRTEM and HR-HAADF) and spectroscopic techniques (X-EDS and STEM-EELS) were combined with image and elemental maps simulations to determine the exact nature of the phases present in the different samples, as well as to try to identify those responsible for both the improved and deteriorated redox responses.

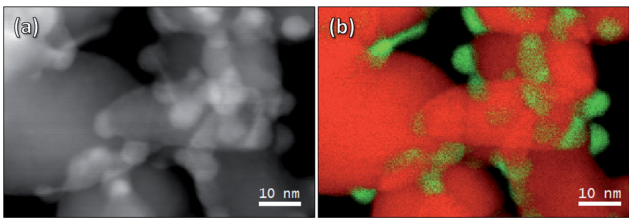

Fig. 2 (a) HAADF image of the CeO_2/TiO_2-fresh sample. (b) Elemental X-EDS map of the image presented in (a), displaying Ti in red and Ce in green color.

Fresh catalyst. As illustrated in Fig. 2, STEM-HAADF studies show the presence of nanosized particles, brighter areas, dispersed over the surface of larger crystallites depicting lower intensity (Fig. 2a). The elemental X-EDS map in Fig. 2b, indicates that the bright areas correspond to a Ce-containing phase, CeO_2, as shown later. Note that the size of CeO_2 particles lies in the 5–10 nm range. The analysis of the HRTEM images of the nanoparticles evidences structural relationships that involve a good match at some of the CeO_2–TiO_2 interfaces. In particular, the following epitaxial relationship is observed between the CeO_2 nanoparticles and the TiO_2 anatase support: $(200)CeO_2//(11\bar{2})TiO_2$; $[010]CeO_2//[111]TiO_2$ (Fig. S4†). These results, obtained on a sample prepared by the microwave-assisted hydrothermal synthesis are in good agreement with the

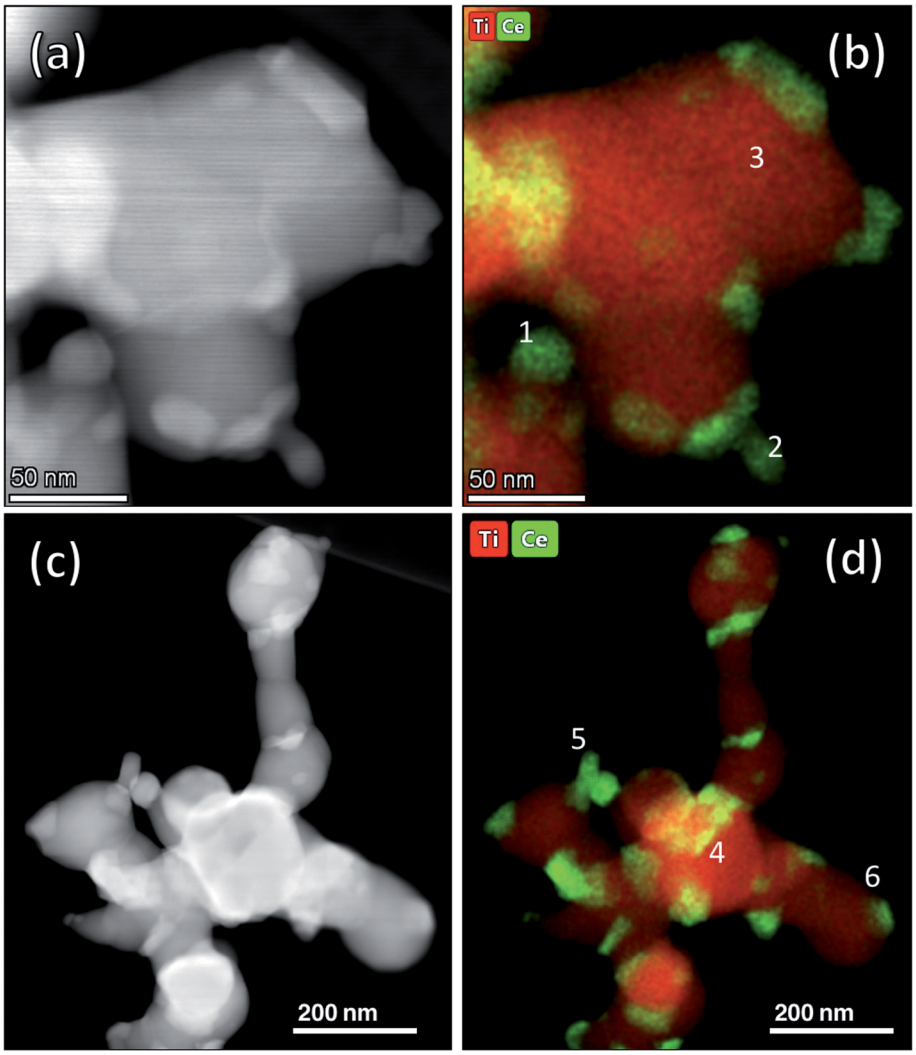

Fig. 3 (a) Representative HAADF image of the CeO_2/TiO_2-SRMO-1C sample. (b) X-EDS elemental map from the previous HAADF image. (c) HAADF image corresponding to the CeO_2/TiO_2-SRMO2-3C sample together with the X-EDS map (d) in both elemental maps, titanium is displayed in red and cerium in green.

 This journal is © The Royal Society of Chemistry 2022

Open Access Article. Published on 09 June 2022. Downloaded on 12/9/2025 12:56:09 PM.
This article is licensed under a Creative Commons Attribution 3.0 Unported Licence.

nanostructures reported by Johnston-Peck *et al.*[29] and Luo *et al.*[30] for a sample with the same cerium loading but prepared using the incipient wetness impregnation method. They described the same epitaxial relationship viewed from a 90° rotated orientation as $(200)CeO_2//(11\bar{2})TiO_2$, $[100]CeO_2//[110]TiO_2$.

Besides the presence of nanoparticles, Johnston-Peck[29] and Luo[30] also indicate other nanostructures of cerium, such as chains and clusters, particularly in samples with lower amounts of the lanthanide element. Such a variety of nanostructures may explain the large width of the redox profile of this sample, which in fact spans the 360–800 °C temperature range.

SRMO samples. Fig. 3 provides a general view of the STEM study of CeO_2/TiO_2-SRMO-1C (a and b) and CeO_2/TiO_2-SRMO2-3C (c and d). The X-EDS maps (Fig. 3b and d) indicate that supported particles of different compositions are present in these samples, which is in good agreement with the brightness variations observed in the corresponding areas of the HAADF images. Table 1 shows quantitative compositional data, in atomic percentages, from different points (1 to 6) in these catalysts, representative of those observed from studies covering a large number of areas. Quantifications from areas corresponding to large crystallites (points 3 and 4) suggest the existence of pure titanium oxide, whereas those corresponding to smaller and brighter areas in the HAADF images indicate the presence of cerium–titanium mixed oxides (positions 1, 2, 5 and 6). In particular, two Ce/Ti molar ratios were observed, 1 : 1 (2 and 5) and 1 : 2 (1 and 6). The deviations from the exact ratios to higher Ti contents are due to the fact that the corresponding particles of the mixed phases are supported onto TiO_2 crystallites. The main difference observed between CeO_2/TiO_2-SRMO-1C and CeO_2/TiO_2-SRMO2-3C refers just to the size of the crystallites, which is larger in CeO_2/TiO_2-SRMO2-3C due to the long exposure of the latter to high-temperature conditions, Fig. S1.†

A detailed analysis of the CeO_2/TiO_2-SRMO-1C and CeO_2/TiO_2-SRMO2-3C samples, using HRTEM and HR-HAADF allowed the identification of the nature of the mixed oxides. Fig. 4a illustrates a representative HR-HAADF image showing an ordered arrangement of Ce and Ti in the lattice of the mixed oxide crystallite. Among all the cerium–titanium mixed oxide phases reported in the literature, the $Ce_4Ti_9O_{24}$ structure is the only one that explains the reflections observed in the Fast Fourier Transform (FFT) (inset in Fig. 4a) of this image. Fig. 4b illustrates a rotated zoom from the image area marked with a yellow dashed square. As indicated, the contrasts can be interpreted as those expected for the [001] projection of the $Ce_4Ti_9O_{24}$ structure. The yellow spots shown as inset locate the positions of the Ce atomic columns in this phase. This interpretation was further confirmed by image simulation, Fig. 4c. A very good agreement was observed with the experimental image, after applying a Gaussian blurring filter to take into account the actual experimental conditions and the presence of noise. Note that these effects lead to a loss of definition of the contrasts corresponding to the Ti atomic columns, which are in fact hardly observed in the experimental image. Furthermore, the intensity profile recorded along the red arrows (Fig. 4e) feature, in the case of the simulated image, several weak shoulders marked with black arrows in the topmost profile, which correspond to the projection of Ti columns. These shoulders are observed only as a slight asymmetry in the corresponding profiles of both the Gaussian-blurred simulated and experimental images.

The HR-HAADF image in Fig. 5a can also be interpreted as being due to the same phase. The FFT analysis (inset in the image) indicates that this $Ce_4Ti_9O_{24}$ particle is oriented along the [010] direction. An EELS-SI study was conducted at the region corresponding to the surface of the nanoparticle (dashed square). The Ce : Ti molar ratio quantified from this SI was very close to 4 : 9, confirming the $Ce_4Ti_9O_{24}$ composition. The correlation between the ADF image, acquired simultaneously with the EELS signal (Fig. 5b), and the Ce-$M_{4,5}$ (green) and Ti-$L_{2,3}$ (red) elemental distributions (Fig. 5c), suggests that cerium is located in the brightest regions of the ADF image, as expected, whereas titanium columns are imaged as the dark areas. The simulated EELS map shown in Fig. 5d confirms this interpretation. ESI† HRTEM and EELS data presented in Fig. S5† evidence the presence of a second perovskite-type Ce–Ti mixed oxide phase, $Ce_2Ti_2O_7$. These results, therefore, reveal the formation of cerium–titanium mixed oxides of two different compositions, $Ce_4Ti_9O_{24}$ and $Ce_2Ti_2O_7$, after the application of an SRMO treatment (either CeO_2/TiO_2-SRMO-1C or CeO_2/TiO_2-SRMO2-3C).

Additional information about these mixed oxides has been extracted from a more detailed ELNES analysis of the Ti-$L_{2,3}$ edge (Fig. S6†). As it is well known, the tetragonal distortion of the coordination environment of Ti, which occurs in both pure anatase and rutile produces a loss of degeneracy in the e_g level. As shown in this figure, this induces a splitting of the L_3 edge into the so-called b and b′ peaks.[45] The rutile polymorph exhibits a shoulder on the b position and an intense peak on the position b′, whereas anatase features an intense peak on b followed by a smooth b′ shoulder. Interestingly, no splitting of the L_3 edge is observed in the EELS spectra acquired on crystallites of the $Ce_4Ti_9O_{24}$ or $Ce_2Ti_2O_7$ mixed oxides. This modification of the fine structure suggests that the incorporation of cerium into the structure is accompanied by a rearrangement of the titanium coordination environment, which finally exhibits lower symmetry (*e.g.* trigonal[46]) than that in the pure TiO_2 phases.

In addition to the two mixed oxide phases described in the previous paragraphs, STEM-EELS experiments performed on the CeO_2/TiO_2-SRMO-1C and CeO_2/TiO_2-SRMO2-3C samples have unveiled the presence of another type of cerium-

Table 1 X-EDS elemental quantification

Position	At% Ti	At% Ce
1	64.4	35.6
2	55.8	44.2
3	94.2	5.8
4	93.9	6.1
5	52.5	47.5
6	68.8	31.2

Open Access Article. Published on 09 June 2022. Downloaded on 12/9/2025 12:56:09 PM.
This article is licensed under a Creative Commons Attribution 3.0 Unported Licence.

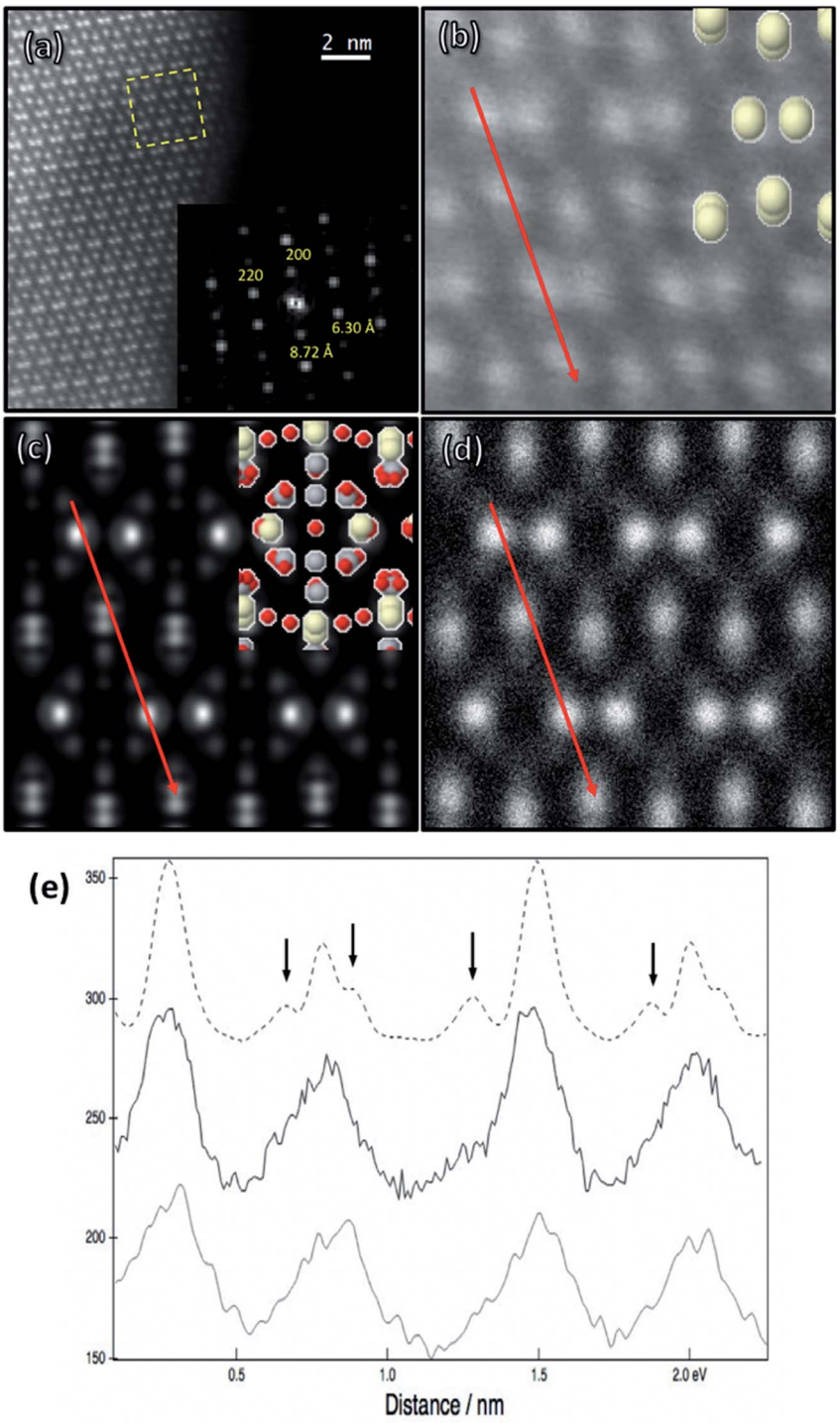

Fig. 4 (a) HR-HAADF image of a $Ce_4Ti_9O_{24}$ particle oriented along the [001] direction. An indexed DDP is shown as inset. (b) Enlargement of the marked area of the experimental image, depicting the overlapped Ce atomic columns. (c) $Ce_4Ti_9O_{24}$ simulated image along [001]. An atomic model of the structure is included as inset (O-red, Ti-grey and Ce-yellow). (d) Simulated image after modification with a Gaussian-blur filter (σ = 2) and electronic noise (σ = 25). (e) Intensity profiles along the red arrows in the simulated (top), Gaussian-blurred simulated (middle) and experimental (bottom) images.

containing nanostructure: an ultrathin layer, which extends over TiO_2 surfaces and interfaces, Fig. 6. These unique nanostructures correspond to the very bright lines observed in the HAADF image shown in Fig. 6a. EELS-SI studies have confirmed this interpretation, Fig. 6b–f. Thus, the Ce-$M_{4,5}$ elemental map corresponding to the area marked in Fig. 6b, indicates that Ce is present not only in large crystallites, like those observed in the lower part of the map but also as a very thin structure covering the surface of TiO_2 support crystallites, Fig. 6c.

 This journal is © The Royal Society of Chemistry 2022

Open Access Article. Published on 09 June 2022. Downloaded on 12/9/2025 12:56:09 PM.
This article is licensed under a Creative Commons Attribution 3.0 Unported Licence.

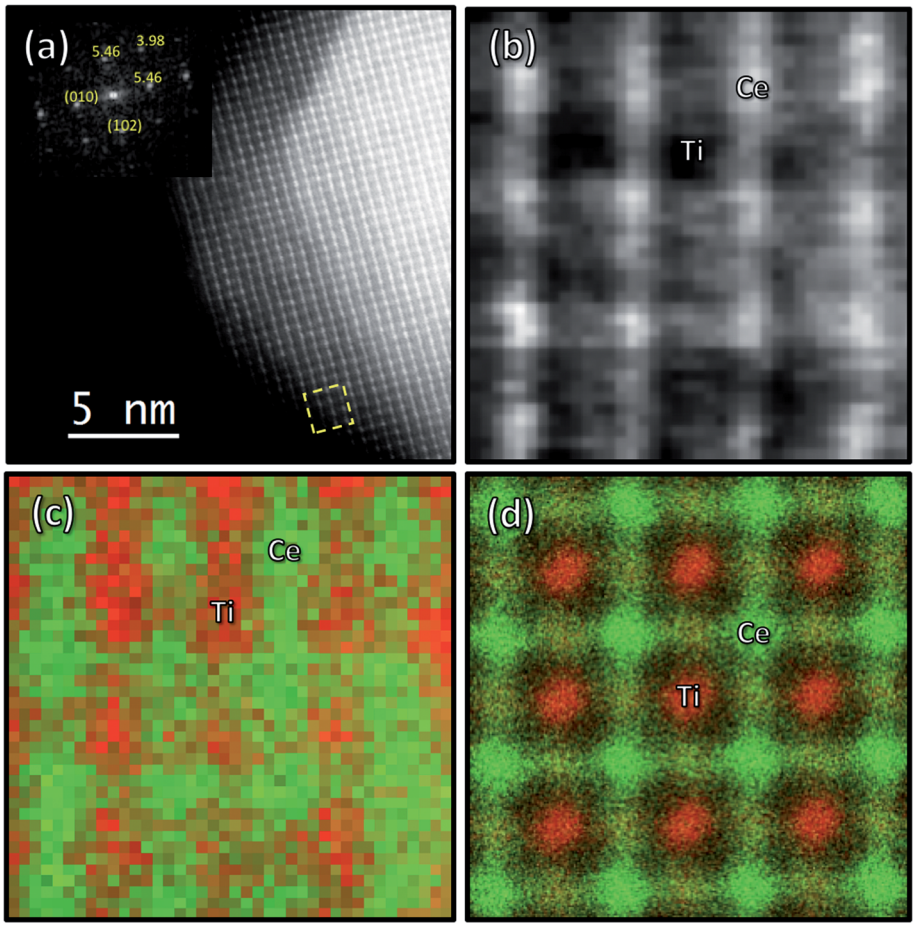

Fig. 5 (a) HR-HAADF image recorded on CeO_2/TiO_2-SRMO-1C illustrating the cationic order in a $Ce_4Ti_9O_{24}$ structure, (FFT of the whole image shown as inset). (b) ADF corresponding to the EELS-SI analysis performed in the area marked with the yellow dashed box. (c) Overlaid Ce-$M_{4,5}$ (green) and Ti-$L_{2,3}$ (red) EELS maps. (d) $Ce_4Ti_9O_{24}$ [010] EELS simulated map overlaying the Ce-$M_{4,5}$ (green) and Ti-$L_{2,3}$ (red) signals.

As shown in Fig. 6d and e, this ultrathin Ce-containing layer occasionally appears as coherently grown onto the surface of TiO_2. In this case, the HR-HAADF image, Fig. 6d, can be interpreted as that of a rutile crystallite along the [001] zone axis. However, the spectrum-image recorded on areas containing the (100) surface, as that marked with a green-dashed box, leads to a Ce-$M_{4,5}$ map, Fig. 6e, which reveals a large concentration of cerium along the surface. Importantly, the thickness of this surface structure is close to that corresponding to just a single atomic layer. The comparison of the spectra registered at the surface (position 1) and at a bulk site (position 2), Fig. 6f, also confirms the presence of the Ce-$M_{4,5}$ edge features just on the surface.

No mismatch was observed between the Ce-containing single atomic surface layer and the underlying TiO_2 support in the HAADF image. Since the crystallite is imaged in this case edge-on, the layer could be in principle the result of the integration of isolated Ce atoms at random sites of the (100) rutile surface. The projection conditions would result in this case in an apparently continuous layer.

Nevertheless, the detailed analysis of HR-HAADF images in which these surface layers are observed from the top, similar to that in Fig. 7, suggests that at least in some cases they correspond to a single, slightly compressed, CeO_2 monolayer. In particular, the comparison of the experimental HAADF image in Fig. 7a with the simulations in Fig. 7b–d illustrates this conclusion.

Note, in this respect, the FFT of Fig. 7a depicts a set of equivalent reflections at 60° and lattice spacing of roughly 3.0 Å, Fig. 7e. Fig. 7b–d show simulated HAADF images for structural models comprising 1, 2 and 3 (111)-CeO_2 layers, respectively, but considering a slightly compressed lattice parameter of 5.11 Å, instead of the 5.41 Å value characteristic of bulk CeO_2.

Though a simple, naked eye, a comparison of the simulations with the experimental HAADF image clearly suggests the best match for the model corresponding to just one (111) layer, Fig. 7b, this is more rigorously confirmed by the analysis of the spatial frequency components of each image. Thus, the FFT of this simulation, Fig. 7f, depicts reflections at 60° and lattice spacings of 3.1 Å, similar to those observed in Fig. 7e. In contrast, the FFT of the model corresponding to 2 (111) layers stacked in A–B sequence, Fig. 7g, shows additional reflections at 1.8 Å, which would correspond to the $(20\bar{2})$ planes in this slightly compressed CeO_2, not observed in the experimental

Open Access Article. Published on 09 June 2022. Downloaded on 12/9/2025 12:56:09 PM.
This article is licensed under a Creative Commons Attribution 3.0 Unported Licence.

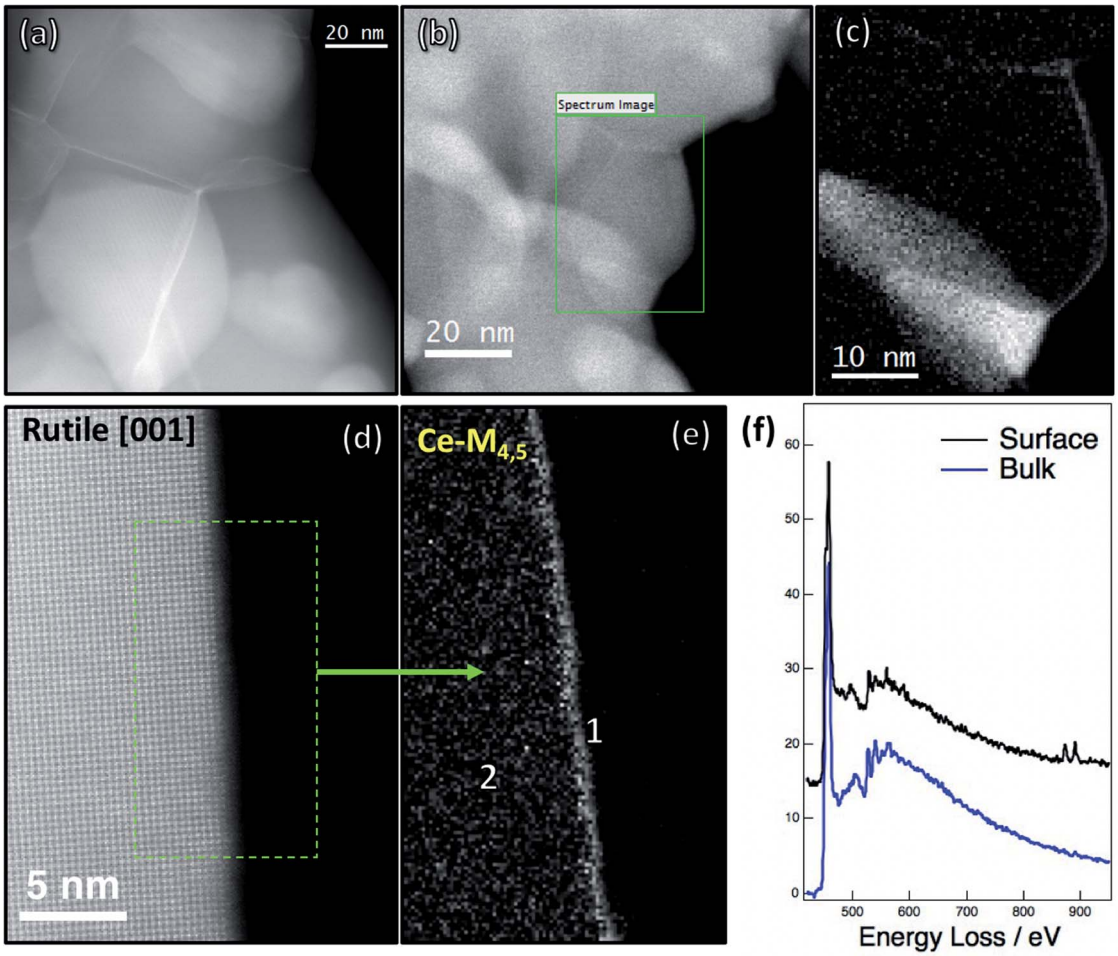

Fig. 6 (a) Low magnification HAADF image characteristic of the CeO_2/TiO_2-SRMO-1C and CeO_2/TiO_2-SRMO2-3C samples. (b) Low magnification HAADF image with a green box indicating the area where the SI study was performed. (c) Ce-$M_{4,5}$ EELS elemental map extracted from the SI. (d) Atomically-resolved HAADF image of a rutile crystal along the [001] direction. The dashed rectangle indicates the region where additional SI was performed; (e) Ce-$M_{4,5}$ EELS elemental map extracted from the SI. (f) Spectra extracted from surface (black) and bulk (blue) locations of the crystallite in (d).

FFT. Finally, these $(20\bar{2})$ reflections are the only ones observed in the FFT of the model with 3 (111) layers stacked in the A–B–C sequence, characteristic of fluorite, Fig. 7h.

As illustrated in Fig. S7,† the 3.1 Å reflections observed in the FFT of the 1 (111) model correspond to 1/3 $(4\bar{2}\bar{2})$ fluorite CeO_2 reflection, which is the basic spatial frequency present in this particular arrangement, is equivalent to (100) reflection for the trigonal A-Ce_2O_3 structure. In the 2 (111) CeO_2 plane model, the frequency corresponding to $(20\bar{2})$ planes for the fluorite structure was also present. Finally, $(20\bar{2})$ is the only frequency detected in the 3 (111) layer model. These results importantly indicate that HR-HAADF does not only allow detecting a single CeO_2 monolayer but also that the analysis in the frequency domain allows distinguishing it from other unique nanostructures such as those of bi- or trilayers. Similarly, the analysis of the FFTs evidenced how the diffraction pattern of 2D materials can change not only in terms of intensity, as has been reported for graphene-related systems but also to show extra reflections at varying distances.[47,48]

Finally, it is also important to stress that the lattice compression detected in the experimental images of the TiO_2-supported ceria monolayer agrees with previous DFT calculations for both standalone (111) CeO_2 monolayers and CeO_2 monolayers grown on YSZ.[49] The question now arises about which of the phases detected in the STEM study of the SRMO samples is responsible for the improvement in low-temperature reducibility observed in the TPR experiments. Particularly, if such a change in the redox behaviour of the material is linked to the mixed oxide phases or, instead, to the ultrathin layers located at the surfaces and interfaces between TiO_2 crystallites.

To clarify this point, the actual oxidation state of Ce and Ti in the different phases was determined by the analysis of the fine structural features of the Ce-$M_{4,5}$ and Ti-$L_{2,3}$ edges from spectra obtained in an EELS SI study.

Fig. 8a shows the ADF image of one region of the CeO_2/TiO_2-SRMO-1C, analogous to the CeO_2/TiO_2-SRMO2-3C sample, where a SI experiment was performed. Ce and Ti maps, Fig. 8b, evidence the presence of a cerium–titanium mixed oxide

 This journal is © The Royal Society of Chemistry 2022

Open Access Article. Published on 09 June 2022. Downloaded on 12/9/2025 12:56:09 PM.
This article is licensed under a Creative Commons Attribution 3.0 Unported Licence.

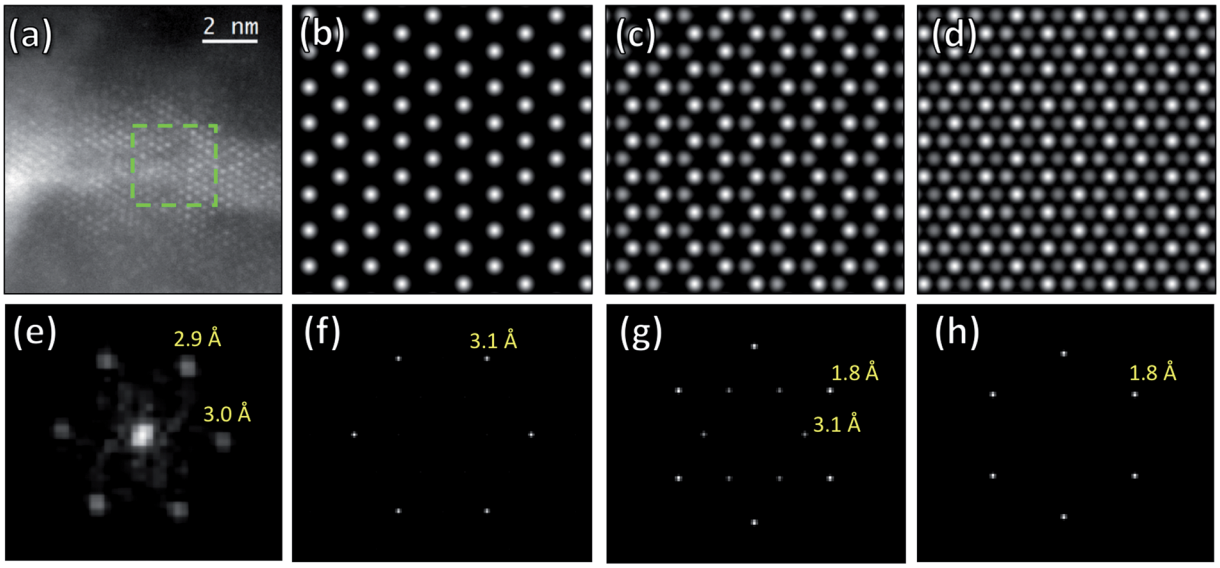

Fig. 7 (a) Experimental HAADF of the CeO_2/TiO_2-SRMO-1C sample illustrating a CeO_2 monolayer, together with the FFT (e) calculated over the green box. (b) Simulated HAADF image corresponding to a single CeO_2 monolayer and its FFT (f). (c) Simulated HAADF image of two CeO_2 monolayer and the corresponding FFT (g). (d) HAADF simulated image corresponding to three CeO_2 monolayer (unit cell) giving rise to the 1.9 reflections of the (111) planes, as observed on its FFT (h).

particle deposited over the corner of a large TiO_2 crystallite. As already described, Ce is also present in this region in the form of an extended ultrathin layer, covering the surface of the TiO_2 crystallite. The Ce-$M_{4,5}$ signal of SI was fitted to Ce^{3+} and Ce^{4+} EELS references acquired under the same experimental conditions, to determine the spatial distribution of each oxidation state. The phase map corresponding to Ce^{3+} shown in Fig. 8c, clearly demonstrates that the supported mixed oxide incorporates Ce only in its reduced state, in good agreement with the chemical formulation deduced for both structures, $Ce_4Ti_9O_{24}$ and $Ce_2Ti_2O_7$, from the structural data.

Regarding the Ce-containing surface layer, the Ce^{3+}/Ce^{4+} maps also point out Ce^{3+}. However, beam-induced reduction of such thin structures cannot be fully disregarded.

To complete the analysis of the Ce oxidation states in this sample, Fig. 8d–f shows EELS results from other regions of the catalysts where the ultrathin layers are located in the grain boundary between two TiO_2 crystallites. The ADF image shows once more, as expected, a bright line between the two TiO_2 crystals, Fig. 8d. Spectra from positions 1 and 2, inset in Fig. 8d, evidence a change in the oxidation state of this element Ce, depicted by the peculiar shift in the energy of the $M_{4,5}$ peaks.

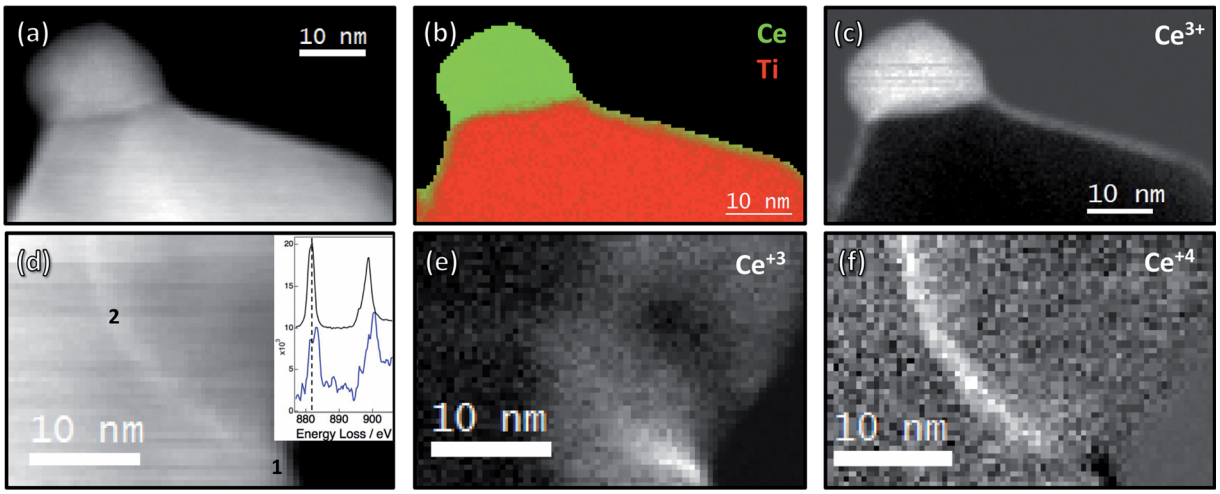

Fig. 8 (a) Representative HAADF image of the CeO_2/TiO_2-SRMO-1C and CeO_2/TiO_2-SRMO2-3C samples, where a SI has also been acquired. (b) Elemental mapping of Ce-$M_{4,5}$ (green) and Ti-$L_{2,3}$ (red) along the analyzed area. (c) Spatial distribution of reduced cerium after fitting the Ce^{3+} EELS reference to the SI. (d) Another region of the CeO_2/TiO_2-SRMO-1C and CeO_2/TiO_2-SRMO2-3C samples showing an interface between two TiO_2 crystals where a SI has been registered. The inset graph displays EELS spectra extracted from the SI positions corresponding to 1 (surface, black spectrum) and 2 (interface, blue spectrum) locations. (e) Spatial distribution of Ce^{3+}. (f) Spatial distribution of Ce^{4+}.

Open Access Article. Published on 09 June 2022. Downloaded on 12/9/2025 12:56:09 PM.
This article is licensed under a Creative Commons Attribution 3.0 Unported Licence.

Position 1, closer to the surface, reveals the characteristic details corresponding to reduced cerium, whereas the spectrum from position 2, at the interface between the two crystals, exhibits a splitting of its first peak and also a shift to higher energies of the second one. Fig. 8e and f, corresponding to the two oxidation states, also provide evidence that the layer is composed nearly in its total length by Ce^{4+}. Only at locations close to the surface, Ce^{3+} is dominating. This peculiar distribution of oxidation states for the same nanostructure reinforces the idea that the presence of Ce^{3+} might very likely be related to the reduction of Ce^{4+} under the electron beam. This process is expected to be more severe for a surface structure than for the one embedded between two TiO_2 crystallites. In fact, highly dispersed surface cerium oxide could be particularly reducible under the electron beam even at beam currents below 30 pA. Thus, Turner *et al.* reported the reduction of the topmost atomic planes in CeO_2-nanocubes,[50] even though they did not discuss electron beam effects.

To back up the results observed at the nanoscale level for the SRMO sample, especially those extracted from EELS and ELNES analysis related to the oxidation state of the lanthanide, macroscopic measurements of surface chemistry were also carried out through XPS experiments (Fig. S8†). The first result worth commenting on is related to the Ce/Ti molar ratio values determined for the CeO_2/TiO_2-fresh and CeO_2/TiO_2-SRMO-1C samples, 0.202 and 0.195, respectively. Both numbers are much higher than that corresponding to the macroscopic value measured by ICP-AES, 0.052, which is fully consistent with the concentration of Ce on the surface. The tiny difference observed before and after the SRMO treatment very likely stems from the small fraction of Ce atoms at the core of the Ce–Ti perovskite crystallites formed after SRMO, which lay beyond the depth of analysis of XPS.

In addition, angle-resolved XPS experiments were performed on the CeO_2/TiO_2-SRMO-1C to further examine the distribution of Ce. Although moderate, a slight increase in the Ce concentration at grazing angles was observed (Fig. S8d†). This trend is expected for an ultrathin, highly dispersed, Ce supported on a much thicker TiO_2 support.

Finally, to explore the oxidation state of the lanthanide in CeO_2/TiO_2-fresh and CeO_2/TiO_2-SRMO-1C, high resolution spectra covering the Ce 3d edge were analysed. To minimize X-ray induced reduction effects, a short exposure time, 8 minutes, was employed. The deconvolution of the different signals in the Ce 3d energy range leads to Ce^{3+}/Ce^{4+} molar ratios of 0.20 and 0.41 for the fresh and SRMO samples, respectively. It is clear that, according to the macroscopic TPR-TCD results, radiation-induced damage could not be overcome, particularly in the much more reducible, CeO_2/TiO_2-SRMO-1C catalyst. The higher, two-fold, values of the Ce^{3+}/Ce^{4+} ratio observed in this case results from both the improved reducibility of this catalyst, as observed in the TPR experiments and the presence of the Ce–Ti perovskite phases revealed by HR-STEM.

The whole set of results of TPR experiments and oxidation state analysis by ELNES/EELS and XPS suggest that highly dispersed CeO_2, in the form of extended monolayers supported on the surface of TiO_2 crystallites, should be responsible for the improvement of reducibility at low temperatures. On the other hand, there is a Ce fraction that remains to form bulk-type mixed oxides. These $Ce_4Ti_9O_{24}$ and $Ce_2Ti_2O_7$ nanoparticles block the lanthanide in its reduced state, even after mild oxidation, in such a way that they cannot contribute to the reducibility of the material. Such fraction must, in fact, be responsible for the decrease in the amount of H_2 consumption observed in the TPR profiles after the SRMO treatments.

In contrast with the reoxidation of the perovskite proposed by Otsuka-Yao-Matsuo *et al.*,[25] our characterization through TPR and advanced electron microscopy indicates that the mixed oxides remain in their reduced state after oxidation up to 500 °C in O_2 (5%)/He.

SRSO sample. Finally, CeO_2/TiO_2-SRSO-2C was also characterized to investigate the structural effects of increasing the temperature of the final oxidation treatment and their correlation with the redox response.

The HAADF images of this catalyst, shown in Fig. 9a, are similar to those of the SRMO samples in Fig. 3a and c. However, as indicated by the quantitative values obtained from the STEM-XEDS analysis, Fig. 9b, the spatial distribution of Ce and Ti is quite different. Only TiO_2 and large CeO_2 particle crystals (content higher than 90–95%) are observed in this sample. No mixed oxides were detected.

The fine structure features of the Ti-$L_{2,3}$ edge also indicate the absence of Ce–Ti mixed oxide phases. Moreover, there is no evidence of anatase in the EEL spectra recorded after the SRSO treatment, as the expected ELNES structure corresponds to the rutile phase (Fig. S9†). Further evidence of the absence of cerium–titanium mixed oxides is also provided by the Ti-$L_{2,3}$ edge maps extracted from the SI-EELS performed on the sample (Fig. S9†). This analysis has also revealed that, after the SRSO thermal treatment, there is no evidence of the anatase structure, which is expected to transform into rutile after high-temperature treatments.

HREM images of the Ce-containing particles at the surface of the TiO_2 crystals confirmed the fluorite structure characteristic of CeO_2. Fig. S10† shows one of these CeO_2 aggregates along the [110] direction.

Finally, EELS analysis across the surface of TiO_2 crystals confirmed the absence of Ce surface species, such as those in the ultrathin layers detected in the SRMO samples.

The absence of the ultrathin ceria layers would explain the lack of reducibility at low temperatures. In fact, Ce is present in

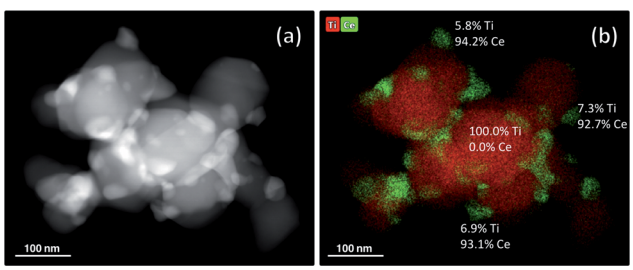

Fig. 9 (a) HAADF image of the CeO_2/TiO_2-SRSO-2C sample. (b) X-EDS maps displaying the spatial distribution of cerium (green) and titanium (red).

 This journal is © The Royal Society of Chemistry 2022

Open Access Article. Published on 09 June 2022. Downloaded on 12/9/2025 12:56:09 PM.
This article is licensed under a Creative Commons Attribution 3.0 Unported Licence.

this SRSO catalyst in the same form as in the fresh CeO_2/TiO_2 sample, though in the form of much bigger CeO_2 particles. This would explain the shift of the reduction events in the TPR profile of the SRSO sample to higher temperatures with respect to the fresh catalyst.[51]

Comparison with CeO_2/ZrO_2 system. The structural response of the CeO_2/TiO_2 system to high-temperature redox cycles shows both similarities and clear differences with respect to that reported for CeO_2/ZrO_2.

For the fresh and SRSO catalysts, both types of formulations consist of 3D-type CeO_2 nanoparticles dispersed over the surface of the support crystallites. The CeO_2 nanoparticles are significantly bigger in the SRSO catalysts, resembling close to those of bulk-type CeO_2. Likewise, the high temperature oxidizing and reducing steps involved in the SRSO treatment promote the transition to the high-temperature polymorph of the support phase, as well as an increase in their crystal size.

Regarding the SRMO treatments, a key common aspect is observed, the appearance of ultrathin, monolayer type, Ce-containing nanostructures, which extend over the surface of the support crystallites. After the SR step, the structure of this surface layer is that of a $Ce_2Zr_2O_7$ pyrochlore in the case of the zirconia-supported catalyst but oxidizes to $Ce_2Zr_2O_8$ after the MO step of the redox cycle. In the CeO_2/TiO_2 system, HR-HAADF and EEL SI reveal the presence of both fluorite type monolayers and Ce-rich monolayers coherently grown onto (100) rutile surfaces. Due to the large structural differences between rutile and CeO_2, these coherent layers must very likely be the result of the incorporation of atomically dispersed Ce species at random positions of the (100) rutile surfaces.

A second significant difference between the structures of the two supported ceria systems after SRMO treatments refers to the growth of mixed oxide phases of different compositions in the CeO_2/TiO_2 system. These phases incorporate the lanthanide in its reduced state, blocking its reoxidation even at temperatures as high as 500 °C, which represents a deleterious influence on the oxygen handling capacity of this type of catalysts.[8,32]

Conclusions

High-temperature redox cycles are shown to induce reversible reducibility modifications in CeO_2/TiO_2 catalysts, similar to those observed in zirconia-supported ones. In particular, reducing treatments at high temperatures led to a significant improvement in low-temperature reducibility. The opposite is observed when the catalysts are treated in oxidizing environments at high temperatures.

Advanced electron microscopy characterization performed on the CeO_2/TiO_2 catalyst has evidenced that although some similarities can be established with the CeO_2/ZrO_2 counterpart, the response to high temperature redox aging treatments of the catalyst supported on titania is much more complex. The largest differences are particularly found between the catalysts reduced at high temperature, *i.e.*, after the SRMO treatments.

The high temperature reduction (SR) followed by mild reoxidation (MO) leads in the CeO_2/TiO_2 system to partial mixing of the two metallic elements into large mixed oxide crystallites of varying Ce : Ti molar ratios ($Ce_4Ti_9O_{24}$ and $Ce_2Ti_2O_7$). Ce^{3+} and Ti^{4+} species become ordered in these phases, whose reoxidation was not observed even at temperatures as high as 500 °C.

An important fraction of Ce (55%) is not incorporated into the mixed oxides but gives rise to atomically thin layers, which are distributed both over the surface and at the grain boundaries between rutile TiO_2 crystallites. Two different structures were detected for these Ce-containing monolayers. In some cases, coherent growth onto the surface of rutile crystallites takes place, which suggests the mixing of Ce with Ti species at the atomic level within the monolayers. However, atomically-thick Ce-containing patches depicting a compressed fluorite type structure have also been observed. EELS SI studies reveal that Ce is present in these monolayers, primarily in its oxidized state, as Ce^{4+}. In any case, the oxidized pyrochlore type phase detected in the catalysts supported on zirconia-based oxides has not been found in the CeO_2/TiO_2 SRMO samples.

On the other hand, SRSO treatments transformed the $Ce_4Ti_9O_{24}$ and $Ce_2Ti_2O_7$ mixed oxides into CeO_2 and rutile-like TiO_2.

The whole set of structural data and the comparison with those of the CeO_2/ZrO_2 system, clearly point out that the improvement in reducibility observed after SRMO is linked to the formation of highly dispersed ceria nanostructures, particularly in the form of extended monolayers. The actual compositional and structural differences between the monolayers formed in the two types of catalyst, CeO_2/ZrO_2 and CeO_2/TiO_2, must be responsible for the differences in the magnitude of the redox improvements observed in each type of system. In this respect, the closer structural relationship between CeO_2 and tetragonal YSZ than that with rutile-type TiO_2 is very likely one of the contributing factors. Besides, differences in the fine details of the electronic states of the monolayers can also lead to differences in their intrinsic capability to activate hydrogen dissociation, which is the key step in the reduction of ceria oxides at low temperatures.[52]

It is also clear that future work should also concentrate on unveiling the thermodynamics and kinetics of the formation of both the mixed Ce–Ti oxides and the Ce-containing layers to be able to find routes to optimize the formation of highly dispersed CeO_2 with enhanced redox properties and avoid the blockage of the lanthanide into the bulk-type mixed oxide phases.

Author contributions

Experiments were carried out by R. M. and supervised by J. A. P.-O. and S. T. Simulations were accomplished by J. M. M.-M. Quantitative TPR experiments were supervised by D. G. Funding was achieved by J. J. C. Finally, R. M. wrote the original draft of the manuscript, and J. A. P.-O., S. T. and J. J. C. reviewed and edited it.

Conflicts of interest

There are no conflicts to declare.

Open Access Article. Published on 09 June 2022. Downloaded on 12/9/2025 12:56:09 PM.
This article is licensed under a Creative Commons Attribution 3.0 Unported Licence.

Acknowledgements

The authors acknowledge funding from the European Union's Horizon 2020 Research and Innovation Program under grant 823717 – ESTEEM3. This work has also received financial support from Junta de Andalucía (FQM334, P20_00968), MINECO/FEDER (Project MAT2017-87579-R) and MCIN/AEI/10.13039/501100011033 (Project PID2020-113006-RB-I00).[53] Electron microscopy studies were performed at the DME-UCA node of the Spanish Unique Infrastructure (ICTS) on Electron Microscopy of Materials ELECMI.

Notes and references

1 A. J. de Abreu, A. F. Lucrédio and E. M. Assaf, *Fuel Process. Technol.*, 2012, **102**, 140–145.
2 A. Kambolis, H. Matralis, A. Trovarelli and C. Papadopoulou, *Appl. Catal., A*, 2010, **377**, 16–26.
3 M. A. Vasiliades, P. Djinović, A. Pintar, J. Kovač and A. M. Efstathiou, *Catal. Sci. Technol.*, 2017, **7**, 5422–5434.
4 D.-W. Jeong, H.-S. Na, J.-O. Shim, W.-J. Jang and H.-S. Roh, *Catal. Sci. Technol.*, 2015, **5**, 3706–3713.
5 M. Boaro, M. Vicario, J. Llorca, C. de Leitenburg, G. Dolcetti and A. Trovarelli, *Appl. Catal., B*, 2009, **88**, 272–282.
6 S. Damyanova, B. Pawelec, K. Arishtirova, M. V. M. Huerta and J. L. G. Fierro, *Appl. Catal., A*, 2008, **337**, 86–96.
7 G. Vlaic, R. Monte, P. Fornasiero, E. Fonda, J. Kaspar and M. Graziani, *Stud. Surf. Sci. Catal.*, 1998, **116**, 185–195.
8 F. Fally, V. Perrichon, H. Vidal, J. Kaspar, G. Blanco, J. M. Pintado, S. Bernal, G. Colon, M. Daturi and J. C. Lavalley, *Catal. Today*, 2000, **59**, 373–386.
9 H. Vidal, J. Kašpar, M. Pijolat, G. Colon, S. Bernal, A. Cordón, V. Perrichon and F. Fally, *Appl. Catal., B*, 2001, **30**, 75–85.
10 R. D. Monte and J. Kašpar, *J. Mater. Chem.*, 2005, **15**, 633–648.
11 S. Trasobares, M. López-Haro, M. Kociak, K. March, F. de La Peña, J. A. Perez-Omil, J. J. Calvino, N. R. Lugg, A. J. D'Alfonso, L. J. Allen and C. Colliex, *Angew. Chem., Int. Ed.*, 2011, **50**, 868–872.
12 C. Karunakaran and P. Gomathisankar, *ACS Sustainable Chem. Eng.*, 2013, **1**, 1555–1563.
13 K. Kasinathan, J. Kennedy, M. Elayaperumal, M. Henini and M. Malik, *Sci. Rep.*, 2016, **6**, 38064.
14 X. Wang, Y. Jin and X. Liang, *Nanotechnology*, 2017, **28**, 505709.
15 C. E. Bamberger, T. J. Haverlock, S. S. Shoup, O. C. Kopp and N. A. Stump, *J. Alloys Compd.*, 1994, **204**, 101–107.
16 A. Dauscher, P. Wehrer and L. Hilaire, *Catal. Lett.*, 1992, **14**, 171–183.
17 M. C. Stennett, C. L. Freeman, A. S. Gandy and N. C. Hyatt, *J. Solid State Chem.*, 2012, **192**, 172–178.
18 A. Verma, A. Goyal and R. K. Sharma, *Thin Solid Films*, 2008, **516**, 4925–4933.
19 A. Preuss and R. Gruehn, *J. Solid State Chem.*, 1994, **110**, 363–369.
20 Z. Gao, L. Liu, X. Han, X. Meng, L. Cao, G. Ma, Y. Liu, J. Yang, Q. Xie and H. He, *J. Am. Ceram. Soc.*, 2015, **98**, 3930–3934.
21 T. Kidchob, L. Malfatti, D. Marongiu, S. Enzo and P. Innocenzi, *J. Sol-Gel Sci. Technol.*, 2009, **52**, 356.
22 L. Kong, D. J. Gregg, I. Karatchevtseva, Z. Zhang, M. G. Blackford, S. C. Middleburgh, G. R. Lumpkin and G. Triani, *Inorg. Chem.*, 2014, **53**, 6761–6768.
23 V. Valeš, L. Matějová, Z. Matěj, T. Brunátová and V. Holý, *J. Phys. Chem. Solids*, 2014, **75**, 265–270.
24 A. I. Leonov, M. M. Piryutko and É. K. Keler, *Bull. Acad. Sci. USSR, Div. Chem. Sci.*, 1966, **15**, 756–760.
25 S. Otsuka-Yao-Matsuo, T. Omata and M. Yoshimura, *J. Alloys Compd.*, 2004, **376**, 262–267.
26 R. Hailili, D. L. Jacobs, L. Zang and C. Wang, *Appl. Surf. Sci.*, 2018, **456**, 360–368.
27 M. Martos, B. Julián-López, J. V. Folgado, E. Cordoncillo and P. Escribano, *Eur. J. Inorg. Chem.*, 2008, **2008**, 3163–3171.
28 D. Schueler, M. Buchert, R. Liu, S. Dittrich and C. Merz, *Study on Rare Earths and Their Recycling, Final Report*, Final Report for The Greens/EFA Group in the European Parliament, 2011.
29 A. C. Johnston-Peck, S. D. Senanayake, J. J. Plata, S. Kundu, W. Xu, L. Barrio, J. Graciani, J. F. Sanz, R. M. Navarro, J. L. G. Fierro, E. A. Stach and J. A. Rodriguez, *J. Phys. Chem. C*, 2013, **117**, 14463–14471.
30 S. Luo, T.-D. Nguyen-Phan, A. C. Johnston-Peck, L. Barrio, S. Sallis, D. A. Arena, S. Kundu, W. Xu, L. F. J. Piper, E. A. Stach, D. E. Polyansky, E. Fujita, J. A. Rodriguez and S. D. Senanayake, *J. Phys. Chem. C*, 2015, **119**, 2669–2679.
31 E. del Río, A. B. Hungría, M. Tinoco, R. Manzorro, M. A. Cauqui, J. J. Calvino and J. A. Pérez-Omil, *Appl. Catal., B*, 2016, **197**, 86–94.
32 C. Arias-Duque, E. Bladt, M. A. Muñoz, J. C. Hernández-Garrido, M. A. Cauqui, J. M. Rodríguez-Izquierdo, G. Blanco, S. Bals, J. J. Calvino, J. A. Pérez-Omil and M. P. Yeste, *Chem. Mater.*, 2017, **29**, 9340–9350.
33 M. P. Yeste, J. C. Hernández-Garrido, D. C. Arias, G. Blanco, J. M. Rodríguez-Izquierdo, J. M. Pintado, S. Bernal, J. A. Pérez-Omil and J. J. Calvino, *J. Mater. Chem. A*, 2013, **1**, 4836–4844.
34 C. Jeanguillaume and C. Colliex, *Ultramicroscopy*, 1989, **28**, 252–257.
35 E. Kirkland, *Advanced Computing in Electron Microscopy*, 1998.
36 L. J. Allen, A. J. D'Alfonso and S. D. Findlay, *Ultramicroscopy*, 2015, **151**, 11–22.
37 S. Bernal, F. J. Botana, J. J. Calvino, C. López, J. A. Pérez-Omil and J. M. Rodríguez-Izquierdo, *J. Chem. Soc., Faraday Trans.*, 1996, **92**, 2799–2809.
38 J. A. Pérez-Omil, **https://temserver.uca.es/global/home/welcome.htm**, 2021.
39 S. Bernal, F. J. Botana, J. J. Calvino, C. López-Cartes, J. A. Pérez-Omil and J. Rodríguez-Izquierdo, *Ultramicroscopy*, 1998, **72**, 135–164.
40 J. El Fallah, L. Hilaire, M. Roméo and F. Le Normand, *J. Electron Spectrosc. Relat. Phenom.*, 1995, **73**, 89–103.
41 E. Paparazzo, *Surf. Sci.*, 1990, **234**, L253–L258.
42 J. Rynkowski, J. Farbotko, R. Touroude and L. Hilaire, *Appl. Catal., A*, 2000, **203**, 335–348.

 This journal is © The Royal Society of Chemistry 2022

Open Access Article. Published on 09 June 2022. Downloaded on 12/9/2025 12:56:09 PM.
This article is licensed under a Creative Commons Attribution 3.0 Unported Licence.

43 F. Giordano, A. Trovarelli, C. de Leitenburg and M. Giona, *J. Catal.*, 2000, **193**, 273–282.
44 Z. Wu, Y. Cheng, F. Tao, L. Daemen, G. S. Foo, L. Nguyen, X. Zhang, A. Beste and A. J. Ramirez-Cuesta, *J. Am. Chem. Soc.*, 2017, **139**, 9721–9727.
45 M. Okada, P. Jin, Y. Yamada, M. Tazawa and K. Yoshimura, *Surf. Sci.*, 2004, **566–568**, 1030–1034.
46 F. M. F. de Groot, M. O. Figueiredo, M. J. Basto, M. Abbate, H. Petersen and J. C. Fuggle, *Phys. Chem. Miner.*, 1992, **19**, 140–147.
47 A. Castellanos-Gomez, L. Vicarelli, E. Prada, J. O. Island, K. L. Narasimha-Acharya, S. I. Blanter, D. J. Groenendijk, M. Buscema, G. A. Steele, J. V. Alvarez, H. W. Zandbergen, J. J. Palacios and H. S. J. van der Zant, *2D Mater.*, 2014, **1**, 025001.
48 Y. Hernandez, V. Nicolosi, M. Lotya, F. M. Blighe, Z. Sun, S. De, I. T. McGovern, B. Holland, M. Byrne, Y. K. Gun'Ko, J. J. Boland, P. Niraj, G. Duesberg, S. Krishnamurthy, R. Goodhue, J. Hutchison, V. Scardaci, A. C. Ferrari and J. N. Coleman, *Nat. Nanotechnol.*, 2008, **3**, 563–568.
49 R. Manzorro, W. E. Celín, J. A. Pérez-Omil, J. J. Calvino and S. Trasobares, *ACS Catal.*, 2019, **9**, 5157–5170.
50 S. Turner, S. Lazar, B. Freitag, R. Egoavil, J. Verbeeck, S. Put, Y. Strauven and G. Van Tendeloo, *Nanoscale*, 2011, **3**, 3385–3390.
51 Q. Fu, A. Weber and M. Flytzani-Stephanopoulos, *Catal. Lett.*, 2001, **77**, 87–95.
52 O. Matz and M. Calatayud, *ACS Omega*, 2018, **3**, 16063–16073.
53 L. A. Bruce, M. Hoang, A. E. Hughes and T. W. Turney, *Appl. Catal., A*, 1996, **134**, 351–362.